

Proposal for noise-free visible-telecom quantum frequency conversion through third-order sum and difference frequency generation

Xiyuan Lu,^{1,2,*} Gregory Moille,^{1,3} Ashutosh Rao,^{1,2} and Kartik Srinivasan^{1,3,†}

¹*Microsystems and Nanotechnology Division, Physical Measurement Laboratory,
National Institute of Standards and Technology, Gaithersburg, MD 20899, USA*

²*Institute for Research in Electronics and Applied Physics and Maryland NanoCenter,
University of Maryland, College Park, MD 20742, USA*

³*Joint Quantum Institute, NIST/University of Maryland, College Park, MD 20742, USA*

Quantum frequency conversion (QFC) between the visible and telecom is a key functionality to connect quantum memories over long distances in fiber-based quantum networks. Current QFC methods for linking such widely-separated frequencies, such as sum/difference frequency generation and four-wave mixing Bragg scattering, are prone to broadband noise from the pump laser(s). To address this issue, we propose to use third-order sum/difference frequency generation (TSFG/TDFG) for an upconversion/downconversion QFC interface. In this process, two pump photons combine their energy and momentum to mediate frequency conversion across visible and telecom bands, bridging a large spectral gap with long-wavelength pump photons, which is particularly beneficial from the noise perspective. We show that waveguide-coupled silicon nitride microring resonators can be designed for efficient QFC between 606 nm and 1550 nm via a 1990 nm pump through TSFG/TDFG. We simulate the device dispersion and coupling, and from the simulated parameters estimate that the frequency conversion can be efficient (> 80 %) at 50 mW pump power. Our results suggest that microresonator-based TSFG/TDFG is promising for compact, scalable, and low power QFC across large spectral gaps.

Quantum frequency conversion (QFC)¹ is an important resource to enable long-distance interconnects between visible wavelength quantum systems, such as optical quantum memories², via telecommunications band fiber links in a quantum network^{3,4}. Efficient and low-noise QFC has typically been shown using the $\chi^{(2)}$ -mediated process of difference (sum) frequency generation for downconversion (upconversion), in particular in situations where the spectral shift required is small enough that the pump field (whose frequency is equal to the spectral shift) is well-separated from the input signal and frequency-converted idler, and is the longest wavelength involved. This configuration, known to yield low-noise performance in platforms like periodically-poled lithium niobate waveguides⁵, has been used in a number of demonstrations, for example, to downconvert 910 nm single photons from a quantum dot to 1550 nm^{6,7}, corresponding to an ≈ 140 THz shift. However, for quantum memories operating at shorter wavelengths, whose spectral separation from the telecom is more than an octave, maintaining the pump as the longest wavelength within a single-stage $\chi^{(2)}$ process is no longer feasible. While QFC to the telecom has been shown in experiments linking a 606 nm rare-earth-ion quantum memory to 1550 nm⁸, as well as 637 nm nitrogen vacancy centers in diamond to 1550 nm⁹, the strong pump field at a spectral location in-between the input signal and output idler (Fig. 1(b)) results in noise (e.g., due to Raman scattering⁵) that is spectrally aligned with the signal/idler and, for example, causes a degradation in antibunched photon statistics⁹. A direct approach is to employ aggressive, narrowband spectral filtering, but typically comes with excessive insertion loss. Other approaches to circumvent this challenge include downconversion to 1310 nm¹⁰ and implementing a two-stage conversion process in which a long wavelength pump is used at each stage¹¹, both circumventing the challenge of direct QFC above an octave.

The $\chi^{(3)}$ nonlinearity has also been studied for QFC via the four-wave mixing Bragg scattering process^{4,12}. Here, the frequency shift is defined by the difference in frequencies of two applied pumps. FWM-BS with single photon states has been demonstrated in both optical fibers¹³) and integrated nanophotonic resonators¹⁴, though the spectral shifts have generally been small (< 20 THz). Recently, FWM-BS has been used to realize frequency conversion between the 1550 nm and 900 nm bands¹⁵, with conversion efficiency exceeding 60 %. However, noise can be a challenge in this scheme, and in general, the large spectral gaps associated with visible-to-telecom conversion necessitate having one of the pumps situated in-between the signal and idler (Fig. 1(c)), similar to the aforementioned discussion in the $\chi^{(2)}$ case. As a result, for visible-telecom QFC using either SFG/DFG ($\chi^{(2)}$) or FWM-BS ($\chi^{(3)}$), to date one always faces the issue of broadband noise from the pump(s) spectrally overlapping with the input and/or output signal.

Thus, while there continue to be significant efforts to mitigate noise and use these existing $\chi^{(2)}$ and $\chi^{(3)}$ approaches to bridge large spectral gaps in QFC experiments, one can also consider whether other nonlinear optical processes might be favorable. For this purpose, we propose to use third-order sum/difference frequency generation (TSFG/TDFG) as an approach for efficient and low-noise QFC between the visible and telecom bands. This process uses two photons from a degenerate infrared pump to make up the spectral gap between the visible and telecom, with a frequency matching equation given by $\omega_v = \omega_t + 2\omega_p$, where $\{\omega_v, \omega_t, \omega_p\}$ represent the visible, telecom, and infrared pump frequencies, respectively. To be concrete, in Fig. 1(a) we consider the visible wavelength of 606 nm (e.g., for a $\text{Pr}^{3+}:\text{Y}_2\text{SiO}_5$ quantum memory¹⁶), a telecom wavelength of 1550 nm, and propose to use a degenerate pump at $\lambda_p = 1990$ nm to make up the spectral difference. A crucial feature of this process, similar to second-order SFG/DFG and FWM-BS, is that each frequency-converted idler photon that is created requires corresponding annihilation of an input signal photon. In contrast, degenerately-pumped four-wave mixing, in which two pump photons are annihilated to

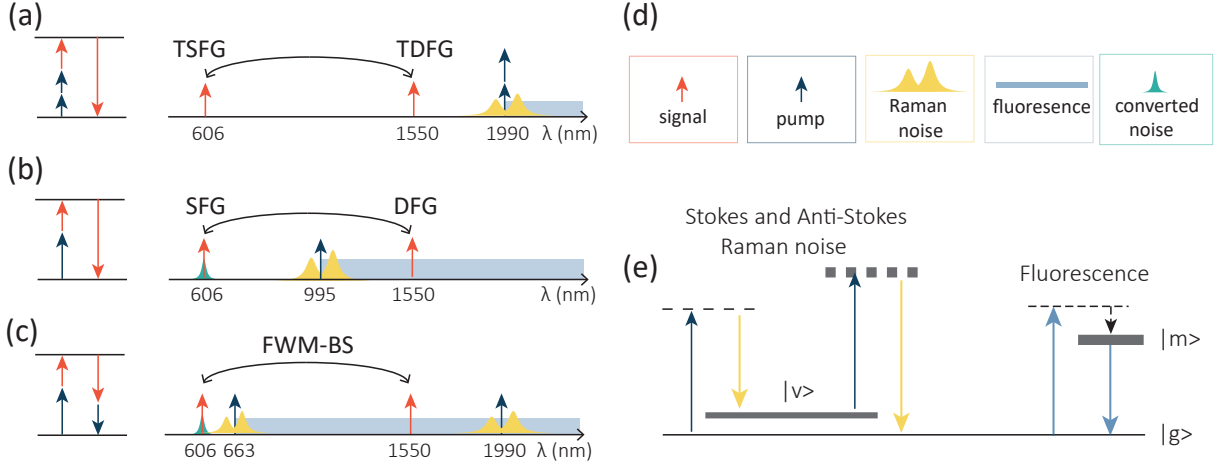


FIG. 1: **Proposal to use third-order sum/difference frequency generation for visible-telecom QFC.** (a) Energy diagrams (left) and operational schemes (right) of the proposed QFC method using third-order sum/difference frequency generation. The arrow length is scaled by energy/frequency in energy diagrams (left) and normalized in wavelength diagrams (right). (b)-(c) Energy diagrams (left) and operational schemes (right) for current methods for visible-telecom QFC, including (b) $\chi^{(2)}$ sum/difference frequency generation (SFG/DFG) and (c) $\chi^{(3)}$ four-wave mixing Bragg-scattering (FWM-BS). (d) Besides the signal (red arrow) and pump laser(s) (blue arrow(s)), there are two types of noise processes under consideration, Raman noise (yellow) and fluorescence noise (blue). Later in the text, we consider the possibility of spontaneous four-wave mixing from the pumps as a third potential noise source. In consideration of these noise sources, TSFG/TDFG is suitable for above-octave-spanning frequency conversion compared to current methods. (e) Schemes of Stokes and anti-Stokes Raman noise and fluorescence noise, where $|g\rangle$, $|v\rangle$, and $|m\rangle$ represent ground, vibrational, and metastable states, respectively. Dashed lines indicate virtual states. Thicker lines indicate broader spectral lineshapes.

create signal and idler photons, can be used to connect widely separated wavelengths^{17,18}, but is inherently unsuitable for QFC because there is no direct conversion from signal to idler, but rather from pump to idler¹². Figure 1 also gives a qualitative indication of how this approach can sidestep broadband noise processes associated with the pump. For $\chi^{(3)}$ media, the main noise processes of concern are Raman scattering, fluorescence, and spontaneous four-wave mixing. As both our input signal and output idler are at higher frequencies than the pump, we anticipate a limited impact from Raman noise or fluorescence. This is in contrast to FWM-BS (Fig. 1(b,bottom)), where the 663 nm pump may be a source of broadband fluorescence. Finally, as we show later, our pump is also situated in the dispersion regime which limits spectral extent over which spontaneous four-wave mixing occurs (so that it does not overlap with the output 1550 nm light).

While TSFG/TDFG is advantageous with respect to the spectral separation of the pump from the signal and idler, it remains to be seen whether this process can be effectively phase- and frequency-matched in a platform suitable for achieving high efficiency. We investigate the TSFG/TDFG process using fully vectorial electromagnetic mode simulations for an integrated silicon nitride (Si_3N_4) microring resonator, a platform that has been established for $\chi^{(3)}$ nonlinear optical processes¹⁹, including those involving widely separated fields, such as third harmonic generation (THG)²⁰, FWM-BS¹⁵, and telecom-visible entangled photon pair generation¹⁷ and classical spectral translation¹⁸.

In a microring, assuming perfect frequency matching and zero laser-cavity detuning, the photon flux/number conversion efficiency of TSFG/TDFG is given by (see supplementary material for derivation):

$$\frac{n_{\text{out}}}{n_{\text{in}}} = \frac{\Gamma_{\text{ct}}\Gamma_{\text{cv}}}{[\Gamma_{\text{tt}}\Gamma_{\text{tv}}/(4\gamma U_{\text{p}}) + \gamma U_{\text{p}}]^2}, \quad (1)$$

where n_{out} and n_{in} are the frequency-converted output photon flux and input signal photon flux in the waveguides, respectively. The conversion efficiency is symmetric for telecom-to-visible and visible-to-telecom conversion, that is, $\{n_{\text{out}}, n_{\text{in}}\} = \{n_{\text{t}}, n_{\text{v}}\}$ or $\{n_{\text{v}}, n_{\text{t}}\}$. $\Gamma_{\text{c}j}$ and $\Gamma_{\text{t}j}$ are the coupling and total decay rate for the j mode. γ represents the $\chi^{(3)}$ interaction strength of TSFG/TDFG. U_{p} is the intra-cavity pump energy, and is related to input pump power by $P_{\text{p}} = (\Gamma_{\text{tp}}/2)^2 U_{\text{p}}/\Gamma_{\text{cp}}$. The number conversion efficiency is optimized at $\Gamma_{\text{ct}}\Gamma_{\text{ci}}/(\Gamma_{\text{tt}}\Gamma_{\text{ti}})$ with an intra-cavity pump energy of $U_{\text{p}} = \sqrt{\Gamma_{\text{tt}}\Gamma_{\text{tv}}}/(2\gamma)$. Importantly, γ depends solely on the device geometry and its modal phase matching scheme, and is proportional to η/V , where η is the mode overlap and V is the averaged mode volume.

Because the frequency span of TSFG/TDFG is similar to that of THG, similar modal phase matching techniques in THG^{20–22} can be used in this work, that is, using high order modes like TE_h5 (transverse-electric mode with five field lobes laterally) or TE_v3 (transverse-electric mode with three field lobes vertically) for visible light²². We here use TE_v3 mode at the visible (≈ 606 nm) as an example for TSFG/TDFG, with pump and telecom both in TE₁ modes. The spatial profiles for these modes

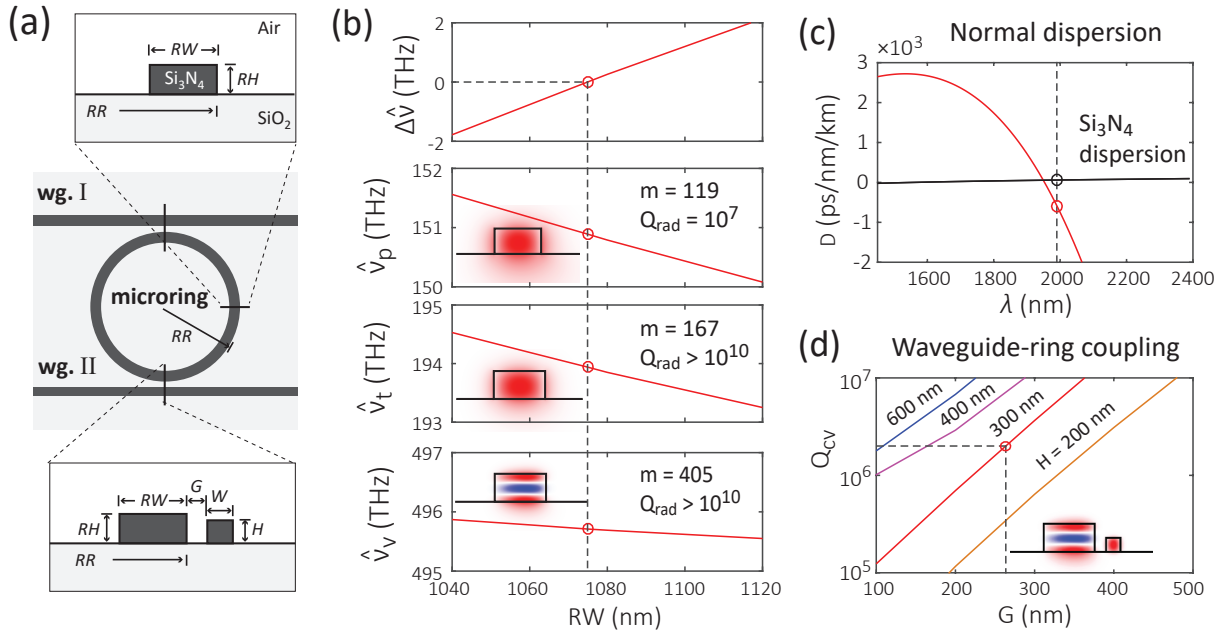


FIG. 2: **TSFG/TDFG design in a Si_3N_4 microring.** (a) Device schematic showing Si_3N_4 microring coupled with two waveguides. The top microring cross-section determines the dispersion design and the bottom microring-waveguide coupling cross-section determines the coupling design. (b) TE1-TE1-TEv3 dispersion design. The pump and telecom are TE1 modes, and the visible is a TEv3 mode (third-order in vertical direction). The nominal parameters are $RR = 25 \mu\text{m}$, $RH = 600 \text{ nm}$, and $RW = 1075 \text{ nm}$. (c) Simulations show that the pump mode has normal dispersion ($D = -580 \text{ ps/nm/km}$, the red circle) at 1990 nm , while the material dispersion is anomalous ($D = 60 \text{ ps/nm/km}$, the black circle). (d) Coupling Q simulation for TEv3 visible mode. A waveguide with $W = H = 300 \text{ nm}$ and $G \approx 270 \text{ nm}$ yields a coupling Q factor (Q_{cv}) of 2×10^6 (dashed lines). Inset shows the coupling geometry.

are shown in Fig. 2(b)-(c). Another example using TEh5 at visible is described in supplementary, whose performance is not as compelling as the TEv3-based scheme. The dispersion design for the TEv3 scheme, or more accurately, TE1-TE1-TEv3 for pump-telecom-visible modes, is shown in Fig. 2(b). The nominal parameters of $RR = 25 \mu\text{m}$, $RH = 600 \text{ nm}$, and $RW = 1075 \text{ nm}$ yield perfect phase matching, that is, momentum conservation in the azimuthal direction for a microring. In particular, the azimuthal mode numbers $\{m_p, m_t, m_v\} = \{119, 167, 405\}$, satisfy $2m_p + m_t = m_v$, and have resonant frequencies near the targeted values. These modes are confirmed to be frequency matched, with a near-zero $\Delta\hat{\nu} = \hat{\nu}_v - \hat{\nu}_t - 2\hat{\nu}_p$ (dashed line). In the nominal design (circles), the pump, telecom, visible modes are at 150.89 THz (1988.23 nm), 193.94 THz (1546.90 nm), and 495.71 THz (605.19 nm), respectively. The simulated radiation-limited optical quality factors (Q_{rad}) are $\approx 10^7$ for the pump mode and $> 10^{10}$ for the visible and telecom modes, so that sidewall scattering will likely be the major limitation for the optical quality factors of these modes in practice. Their averaged mode volume ($\bar{V} = (V_p^2 V_t V_v)^{1/4}$) is calculated to be $61.0 \mu\text{m}^3$ and the mode overlap is 8.5% . Importantly, the dispersion is normal around the pump, as shown in Fig. 2(c), which is beneficial in suppressing optical parametric oscillation²³ and frequency comb generation²⁴, as both processes generally require anomalous dispersion. Their elimination ensures that the pump will be efficiently used for mediating the desired TDFG/TSFG process. It does not necessarily preclude the possibility of spontaneous four-wave mixing (SFWM) from the pump, which can be a noise source if it spectrally overlaps with the converted telecom idler. From energy conservation, this hypothetical SFWM noise process would convert two pump photons at 1988.23 nm to a signal photon at 1546.90 nm and idler photon at 2781.91 nm . For our geometry, however, this process is inhibited, as the ring does not support modes above $\approx 2300 \text{ nm}$, due to cut-off associated with the asymmetric cladding structure.

We choose a top air cladding and bottom SiO_2 substrate for the Si_3N_4 microring (Fig. 2(a)). Such an asymmetric configuration has advantages for both coupling and dispersion. For coupling, long wavelength modes can be cut-off in a narrow waveguide because of this asymmetry, which is necessary to separate the coupling tasks for the widely separated visible and telecom/ $2 \mu\text{m}$ modes¹⁷. For dispersion, the ring radius (RR), ring width (RW), and ring thickness/height (RH) are the three geometric control parameters, as indicated in the top cross-section in Fig. 2(a). In air-clad device, these parameters can be trimmed by dry/wet etching for dispersion tuning¹⁸.

While high- Q , relatively small mode volume, and phase- and frequency-matching ensure efficient intra-cavity conversion, for an overall high on-chip efficiency, efficient resonator-waveguide coupling is needed (see Equation (1)). The waveguide width (W), waveguide height (H), and ring-waveguide gap (G) are three adjustable parameters that, together with the microring geometry, determine the coupling characteristics. A cross-section schematic of the coupling region is shown in Fig. 2(a), and we

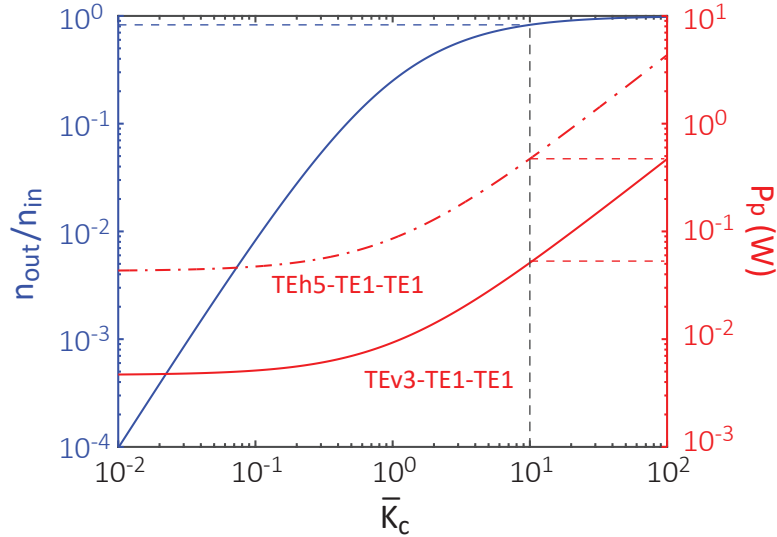


FIG. 3: **Optimized conversion efficiency and required pump powers.** In-waveguide photon flux/number conversion efficiency (blue, left y-axis) as a function of effective coupling ratio ($\bar{K}_c \equiv \sqrt{\Gamma_{ct}\Gamma_{cv}/(\Gamma_{0t}\Gamma_{0v})}$). This efficiency is independent of the scheme (TEv3/TEh5 for the visible mode) and the direction of the frequency conversion (visible-to-telecom, or telecom-to-visible). For example, to achieve a number conversion efficiency of 83 % (the blue dashed line), a \bar{K}_c of 10 is needed (the black dashed line). However, to achieve such efficiency and effective coupling ratio, the power required (red, right y-axis) to operate the TEv3/TEh5 (solid/dot-dashed lines) schemes differs by almost an order of magnitude, requiring 50 mW/470 mW (the red dashed lines), respectively.

use a coupled mode theory formalism²⁵ to determine the coupling quality factor (Q_c) at the three targeted wavelengths, where in all cases the waveguide mode considered is the fundamental TE1 mode. The resonator's TE1 pump (≈ 1990 nm) and telecom modes are easily coupled to the waveguide. For example, a waveguide with $W = 750$ nm and $G = 650$ nm results in $Q_c \approx 2 \times 10^6$. At such a gap, coupling of the visible signal is negligible ($Q_{cv} > 10^9$). We thus use a second waveguide exclusively for coupling of the TEv3 visible mode in the resonator, where its size (width and height) is small enough that, given the asymmetric cladding, the telecom and pump wavelengths are cut-off. As shown in Fig. 2(d), a square waveguide with $W = H = 300$ nm and $G = 270$ nm, which can provide $Q_{cv} = 2 \times 10^6$ (red circle). $Q_{cv} = 2 \times 10^5$ can be achieved by either a closer gap or a shallower waveguide (Fig. 2(f)). To implement such waveguide coupling in practice, a second alignment in the electron beam lithography and a separate shallow-etching process can be used.

Finally, the optimized efficiencies and required pump powers following Equation (1) are shown in Fig. 3, where we assume all optical modes have intrinsic $Q = 2 \times 10^6$, and consider the case where the pump is critically coupled. For the TEv3 design, at 50 mW input power, with an over-coupling of $10\times$, the number conversion efficiency is 83 % (dashed lines in Fig. 3). As noted earlier, stronger overcoupling (either by higher intrinsic Q or lower Q_c) will further increase the conversion efficiency, though the former is preferred as the latter comes at the expense of additional pump power.

In summary, we propose using third-order sum/difference frequency generation (TSFG/TDFG) for noise-free QFC, and provide detailed simulations for realizing such a process in a Si_3N_4 microring. This nanophotonic QFC interface could be particularly useful for building scalable quantum networks. Although we only simulate this process in a microring, TSFG/TDFG can be applied to other platforms, including nanophotonic waveguides and periodically-poled crystals.

Supplementary Information: Theory and Additional Simulation Data

I. THEORY FOR CAVITY-ENHANCED TSFG/TDFG

In this section, we give more details on the equations we provide in the main text, starting with the following coupled mode equations^{26,27}:

$$\frac{d\tilde{A}_p}{dt} = [i(\Delta\omega_p + \gamma_{pppp}U_p) - \Gamma_{tp}/2] \tilde{A}_p + 2i\gamma_{tpv}\tilde{A}_s\tilde{A}_t^*\tilde{A}_p^* + i\sqrt{\Gamma_{cp}}\tilde{S}_p, \quad (2)$$

$$\frac{d\tilde{A}_v}{dt} = [i(\Delta\omega_v + 2\gamma_{vppv}U_p) - \Gamma_{tv}/2] \tilde{A}_v + i\gamma_{vtp}\tilde{A}_p^2\tilde{A}_t + i\sqrt{\Gamma_{cv}}\tilde{S}_v, \quad (3)$$

$$\frac{d\tilde{A}_t}{dt} = [i(\Delta\omega_t + 2\gamma_{tptp}U_p) - \Gamma_{tt}/2] \tilde{A}_t + i\gamma_{tvp}(\tilde{A}_p^*)^2\tilde{A}_v + i\sqrt{\Gamma_{ct}}\tilde{S}_t. \quad (4)$$

As mentioned in the text, the equations already assume perfect phase matching, that is, $m_v = 2m_p + m_t$. The field amplitude is normalized so that $U_i = |\tilde{A}_i|^2$ where $i = \{p, v, t\}$ represents intra-cavity energy for pump, signal and idler, respectively. The first terms describe the cavity evolution considering Kerr shifts. The cavity detuning without Kerr shifts is $\Delta\omega_i = \omega_i - \omega_{i0}$, where ω_{i0} represents the center of the Lorentzian resonances for the i mode. The self/cross phase modulation (SPM/XPM) red-shift/decrease cavity resonance frequencies, depending on pump intra-cavity optical energies (U_p) only, as U_v and U_t are at the quantum level for quantum frequency conversion. Γ_{ti} describes the decay of the intra-cavity energy U_i , which includes the intrinsic cavity loss and the out-coupling to waveguide, $\Gamma_{ti} = \Gamma_{oi} + \Gamma_{ci}$. Here the decay term Γ_{ji} is related to optical quality factor Q_{ji} or the field coupling/decay time τ_{ji} by:

$$\Gamma_{ji} = \frac{\omega_{oi}}{Q_{ji}} = \frac{2}{\tau_{ji}}, \quad (j = t, 0, c; i = p, v, t). \quad (5)$$

The second terms describe the TSFG/TDFG interaction with degenerate pump, signal and idler. Both Kerr shifts and TSFG/TDFG interaction are $\chi^{(3)}$ processes, and the involved nonlinear interaction term γ_{ijkl} is given by:

$$\gamma_{ijkl} = \frac{3\omega_i\eta_{ijkl}\chi_{ijkl}^{(3)}}{4\bar{n}_{ijkl}^4\epsilon_0\bar{V}_{ijkl}}, \quad (\text{with } i, j, k, l = p, v, t), \quad (6)$$

which is a positive real parameter. For simplicity, we here assume the ideal situation of perfect frequency matching after the Kerr effect (the Kerr-shifted cavity detuning is zero). Therefore, we only need to consider the TSFG/TDFG interaction, and we have:

$$\frac{\gamma}{\sqrt{\omega_v\omega_t}} \equiv \frac{\gamma_{pvpt}}{\omega_p} = \frac{\gamma_{vptp}}{\omega_v} = \frac{\gamma_{tpvp}}{\omega_t} = \frac{3\eta_{pptv}\chi_{pptv}^{(3)}}{4\bar{n}_{pptv}^4\epsilon_0\bar{V}_{pptv}}, \quad (7)$$

where γ is used in the main text so that it is independent of telecom or visible modes. The permutation sequence in the last term does not matter. Therefore, we abbreviate the subscripts of \bar{n} , η , \bar{V} , and $\chi^{(3)}$ in the main text. Both η and \bar{V} are calculated from the pump, telecom, and visible mode profiles,

$$\eta = \frac{\int_V dv \epsilon_p \sqrt{\epsilon_v \epsilon_t} \tilde{E}_p^2 \tilde{E}_t \tilde{E}_v^*}{(\int_V dv \epsilon_p^2 |\tilde{E}_p|^4)^{1/2} (\int_V dv \epsilon_v^2 |\tilde{E}_v|^4 \int_V dv \epsilon_t^2 |\tilde{E}_t|^4)^{1/4}}, \quad (8)$$

$$\bar{V} = (V_p^2 V_t V_v)^{1/4}, \quad \text{where } V_i = \frac{(\int_V dv \epsilon_i |\tilde{E}_i|^2)^2}{\int_V dv \epsilon_i^2 |\tilde{E}_i|^4} \quad (\text{with } i = p, t, v). \quad (9)$$

The last terms in these two equations are the source terms for pump and signal, where $P_i = |\tilde{S}_i|^2$ represents the input power in the waveguide.

In perfect cavity detuning and steady state, considering the visible and telecom fields are at the quantum level, and only considering upconversion (where the visible mode has no input), the equations of the cavity fields are reduced to:

$$(\Gamma_{tp}/2)^2 U_p = \Gamma_{cp} P_p \quad (10)$$

$$(\Gamma_{tv}/2)^2 U_v = \gamma_{vtp}^2 U_p^2 U_t \quad (11)$$

$$(\Gamma_{tt}/2 + 2\gamma_{tvp}^2 U_p^2 / \Gamma_{tv})^2 U_t = \Gamma_{ct} P_t \quad (12)$$

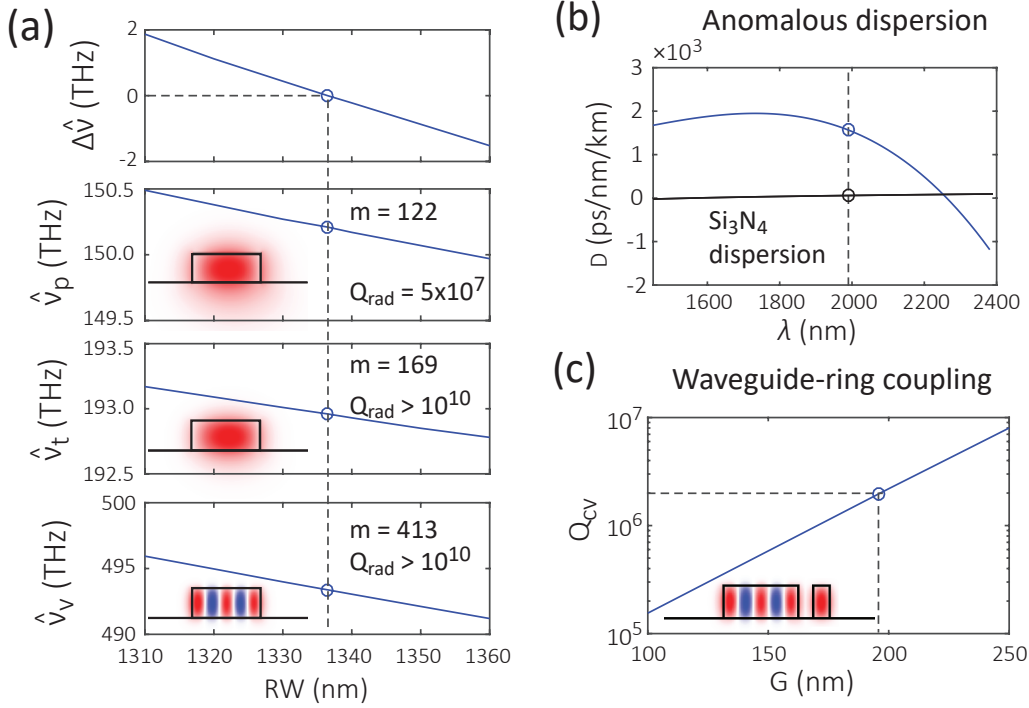


FIG. 4: **An alternative TSFG/TDFG design.** (a) TE1-TE1-TEh5 dispersion design. The mode profiles (radial component of electric field) are shown in the insets, with radiation Q values (Q_{rad}) specified for pump, telecom, and visible modes. The pump and telecom are fundamental transverse-electric-like (TE1) modes, while the visible is a TEh5 mode. The nominal parameters are $RR = 25 \mu\text{m}$, $RH = 600 \text{ nm}$, and $RW = 1337 \text{ nm}$, which leads to perfect frequency matching (circles). (b) Simulation shows that this design exhibits anomalous dispersion around the pump mode at 1990 nm ($D = 1,600 \text{ ps/nm/km}$, the blue circle), and the material dispersion is also anomalous ($D = 60 \text{ ps/nm/km}$, the black circle). This dispersion corresponds to 3.8 GHz (anomalous) in frequency mismatch of the adjacent modes. (c) Coupling Q simulation for TEh5 visible mode. The waveguide with $RW = 300 \text{ nm}$, $RH = 600 \text{ nm}$, and $G \approx 200 \text{ nm}$ has a coupling Q factor (Q_{cv}) of 2×10^6 (dashed lines). Inset shows its microring-waveguide coupling geometry.

The visible output power is the out coupling of the cavity energy, that is:

$$P_v = \Gamma_{\text{cv}} U_v. \quad (13)$$

In combination of Eq. (11) and Eq. (7), we have the intra-cavity photon number ratio as,

$$\frac{N_v}{N_t} = \frac{\omega_t U_v}{\omega_v U_t} = \left(\frac{\gamma U_p}{\Gamma_{\text{tv}}/2} \right)^2. \quad (14)$$

In the waveguide, considering this equation along with Eq. (12) and Eq. (13), we have the number/flux conversion efficiency as:

$$\frac{n_v}{n_t} = \frac{\omega_t P_v}{\omega_v P_t} = \frac{\Gamma_{\text{ct}} \Gamma_{\text{cv}}}{[(\Gamma_{\text{tt}} \Gamma_{\text{tv}} / (4\gamma U_p)) + \gamma U_p]^2}. \quad (15)$$

We can see from Eq. (15) that the number conversion efficiency is optimized with a value of $\Gamma_{\text{ct}} \Gamma_{\text{ci}} / (\Gamma_{\text{tt}} \Gamma_{\text{ti}})$ when the intracavity pump energy satisfies $\gamma U_p = \sqrt{\Gamma_{\text{tt}} \Gamma_{\text{tv}} / 2}$, with pump input power given by Eq. (10). The number conversion efficiency approaches unity (100 %) when both visible and telecom modes are significantly overcoupled ($\Gamma_{\text{tt}} \approx \Gamma_{\text{ct}}$, $\Gamma_{\text{tv}} \approx \Gamma_{\text{cv}}$). Although we have only consider the upconversion case explicitly, the expressions in terms of number ratio/efficiency are the same for downconversion in Eq. 15. Therefore, in the main text, we use $\{n_{\text{out}}, n_{\text{in}}\}$ to represent both cases, that is, $\{n_t, n_v\}$ for downconversion and or $\{n_v, n_t\}$ for upconversion.

II. ADDITIONAL SIMULATION DATA FOR TEH5-TE1-TE1 CONFIGURATION

The dispersion design for the TEh5 scheme, or more accurately, TE1-TE1-TEh5 for pump-telecom-visible modes, is shown in Fig. 4(a). The nominal parameters of $RR = 25 \mu\text{m}$, $RH = 600 \text{ nm}$, and $RW = 1337 \text{ nm}$ yield perfect phase matching, which for a

microring, corresponds to momentum conservation in the azimuthal direction. In particular, the azimuthal mode numbers $\{m_p, m_t, m_v\} = \{122, 169, 413\}$, satisfy $2m_p + m_t = m_v$, and have resonant frequencies near the targeted values. In the nominal design (circles), the pump, telecom, visible modes are at 150.21 THz (1997.20 nm), 192.96 THz (1554.73 nm), and 493.98 THz (608.05 nm), respectively. Their averaged mode volume, given by $\bar{V} = (V_p^2 V_t V_v)^{1/4}$, is calculated to be $71.8 \mu\text{m}^3$ and the mode overlap is 1.1 %. In addition, this device geometry shows anomalous dispersion around the pump ($D = 1,600 \text{ ps/nm/km}$), as shown in Fig. 4(b), which corresponds to 3.8 GHz frequency mismatch in adjacent modes with a 1 THz free spectral range. The larger mode volume and smaller mode overlap, and the anomalous dispersion around the pump make this TEh5 scheme less appealing than the proposed TEv3 scheme. One advantage of the TEh5 scheme is its simplicity in coupling design. As shown in Fig. 4(c), a waveguide with $W = 300 \text{ nm}$ and $G \approx 200 \text{ nm}$ can provide $Q_{cv} = 2 \times 10^6$ (dashed lines). Such a coupling is more straightforward than the TEv3 configuration, and does not require a separate shallow etching process.

Funding. This work is supported by the DARPA DODOS and NIST-on-a-chip programs.

Acknowledgements. X.L. and A.R. acknowledge support under the Cooperative Research Agreement between the University of Maryland and NIST-PML, Award no. 70NANB10H193.

* Electronic address: xiyuan.lu@nist.gov

† Electronic address: kartik.srinivasan@nist.gov

- ¹ P. Kumar, "Quantum frequency conversion," *Opt. Lett.* **15**, 1476–1478 (1990).
- ² A. I. Lvovsky, B. C. Sanders, and W. Tittel, "Optical quantum memory," *Nat. Photon.* **3**, 706–714 (2009).
- ³ H. J. Kimble, "The quantum internet," *Nature* **453**, 1023–1030 (2008).
- ⁴ M. G. Raymer and K. Srinivasan, "Manipulating the color and shape of single photons," *Phys. Today* **65**, 32–37 (2012).
- ⁵ J. S. Pelc, L. Ma, C. R. Phillips, Q. Zhang, C. Langrock, O. Slattery, X. Tang, and M. M. Fejer, "Long-wavelength-pumped upconversion single-photon detector at 1550 nm: performance and noise analysis," *Opt. Express* **19**, 21445–21456 (2011).
- ⁶ K. De Greve, L. Yu, P. L. McMahon, J. S. Pelc, C. M. Natarajan, N. Y. Kim, E. Abe, S. Maier, C. Schneider, M. Kamp, S. Höfling, R. H. Hadfield, A. Forchel, M. M. Fejer, and Y. Yamamoto, "Quantum-dot spin-photon entanglement via frequency downconversion to telecom wavelength," *Nature* **491**, 421–425 (2012).
- ⁷ J. H. Weber, B. Kambs, J. Kettler, S. Kern, J. Maisch, H. Vural, M. Jetter, S. L. Portalupi, C. Becher, and P. Michler, "Two-photon interference in the telecom C-band after frequency conversion of photons from remote quantum emitters," *Nat. Nanotech.* **14**, 23–26 (2019).
- ⁸ N. Maring, D. Lago-Rivera, A. Lenhard, G. Heinze, and H. de Riedmatten, "Quantum frequency conversion of memory-compatible single photons from 606 nm to the telecom C-band," *Optica* **5**, 507–513 (2018).
- ⁹ A. Dréau, A. Tchekorava, A. E. Mahdaoui, C. Bonato, and R. Hanson, "Quantum Frequency Conversion of Single Photons from a Nitrogen-Vacancy Center in Diamond to Telecommunication Wavelengths," *Phys. Rev. Appl.* **9**, 1–8 (2018).
- ¹⁰ S. Zaske, A. Lenhard, C. A. Keßler, J. Kettler, C. Hepp, C. Arend, R. Albrecht, W.-M. Schulz, M. Jetter, P. Michler, and C. Becher, "Visible-to-telecom quantum frequency conversion of light from a single quantum emitter," *Phys. Rev. Lett.* **109**, 147404 (2012).
- ¹¹ V. Esfandyarpour, C. Langrock, and M. Fejer, "Cascaded downconversion interface to convert single-photon-level signals at 650 nm to the telecom band," *Opt. Lett.* **43**, 5655–5658 (2018).
- ¹² C. J. McKinstrie, J. D. Harvey, S. Radic, and M. G. Raymer, "Translation of quantum states by four-wave mixing in fibers," *Opt. Express* **13**, 9131–9142 (2005).
- ¹³ H. J. McGuinness, M. G. Raymer, C. J. McKinstrie, and S. Radic, "Quantum frequency translation of single-photon states in a photonic crystal fiber," *Phys. Rev. Lett.* **105**, 093604 (2010).
- ¹⁴ A. Singh, Q. Li, S. Liu, Y. Yu, X. Lu, C. Schneider, S. Höfling, J. Lawall, V. Verma, R. Mirin, S. W. Nam, J. Liu, and K. Srinivasan, "Quantum frequency conversion of a quantum dot single-photon source on a nanophotonic chip," *Optica* **6**, 563–569 (2019).
- ¹⁵ Q. Li, M. Davanço, and K. Srinivasan, "Efficient and low-noise single-photon-level frequency conversion interfaces using silicon nanophotonics," *Nat. Photon.* **10**, 406–414 (2016).
- ¹⁶ M. P. Hedges, J. J. Longdell, Y. Li, and M. J. Sellars, "Efficient quantum memory for light," *Nature* **465**, 1052–1056 (2010).
- ¹⁷ X. Lu, Q. Li, D. A. Westly, G. Moille, A. Singh, V. Anant, and K. Srinivasan, "Chip-integrated visible-telecom photon pair sources for quantum communication," *Nat. Phys.* **15**, 373–381 (2019).
- ¹⁸ X. Lu, G. Moille, Q. Li, D. A. Westly, A. Rao, S.-P. Yu, T. C. Briles, S. B. Papp, and K. Srinivasan, "Efficient telecom-to-visible spectral translation using silicon nanophotonics," *Nat. Photon.* **13**, 593–601 (2019).
- ¹⁹ D. J. Moss, R. Morandotti, A. L. Gaeta, and M. Lipson, "New cmos-compatible platforms based on silicon nitride and hydrex for nonlinear optics," *Nat. Photon.* **7**, 597–607 (2013).
- ²⁰ J. S. Levy, M. A. Foster, A. L. Gaeta, and M. Lipson, "Harmonic generation in silicon nitride ring resonators," *Opt. Express* **19**, 11415–11421 (2011).
- ²¹ T. Carmon and K. Vahala, "Visible continuous emission from a silica microphotonic device by third-harmonic generation," *Nat. Phys.* **3**, 430–435 (2007).
- ²² J. B. Surya, X. Guo, C.-L. Zou, and H. X. Tang, "Efficient third-harmonic generation in composite aluminum nitride/silicon nitride microrings," *Optica* **5**, 103–108 (2018).
- ²³ T. J. Kippenberg, S. Spillane, and K. J. Vahala, "Kerr-nonlinearity optical parametric oscillation in an ultrahigh-q toroid microcavity," *Phys. Rev. Lett.* **93**, 083904 (2004).

- ²⁴ A. L. Gaeta, M. Lipson, and T. J. Kippenberg, “Photonic-chip-based frequency combs,” *Nat. Photon.* **13**, 158–169 (2019).
- ²⁵ G. Moille, Q. Li, T. C. Briles, S.-P. Yu, T. Drake, X. Lu, A. Rao, D. Westly, S. B. Papp, and K. Srinivasan, “Broadband resonator-waveguide coupling for efficient extraction of octave-spanning microcombs,” *Opt. Lett.* **44**, 4737–4740 (2019).
- ²⁶ Q. Lin, O. J. Painter, and G. P. Agrawal, “Nonlinear optical phenomena in silicon waveguides: Modeling and applications,” *Opt. Express* **15**, 16604–16644 (2007).
- ²⁷ X. Lu, G. Moille, A. Singh, Q. Li, D. A. Westly, A. Rao, S.-P. Yu, T. C. Briles, S. B. Papp, and K. Srinivasan, “Milliwatt-threshold visible–telecom optical parametric oscillation using silicon nanophotonics,” *Optica* **6**, 1535–1541 (2019).